scientific reports

OPEN

Research on enhancing heat transfer in geothermal well cementing via novel expanded graphite and cured epoxy resin composite filler

Wenxi Zhu[1]✉, Bingjie Wang[1], Shengkai Cui[1], Jing Wang[2] & Huijing Tan[3]

Effective heat transfer between the working fluid and subterranean rocks is essential for producing green and low-carbon geothermal energy. As the primary thermal conductive medium, cement has low thermal conductivity, leading to high thermal resistance and significantly reducing geothermal wells' efficiency. Therefore, high thermal conductivity cement has emerged as a widely anticipated new research area. The purpose of this research is to address the substantial harm of traditional carbon-based thermal conductive fillers to cement. A novel expanded graphite (EG)/epoxy resin (EP) composite additive (MEG) was designed to increase cement's thermal conductivity while preserving its mechanical strength and pumpability. Firstly, the physicochemical properties of MEG were revealed by FT-IR, UV-Vis, SEM, and TGA. Then, the applicability of MEG cement in adverse geological environments (high-temperature 60–100 ℃, high-mineralization 5–36% NaCl) was evaluated through simulated maintenance experiments. Finally, the hydration products and pore structure of MEG-cement were analyzed by XRD/FT-IR and SEM/MIP, revealing the thermal conductivity enhancing mechanism. The results showed that: 1) MEG uses ZDMA as a bridge to promote the ring opening and curing of EP, and is formed by strong cation -π interaction with EG. 2)After curing at 60–100 ℃, MEG-cement exhibits a significant increase (46.6-182.1%) in thermal conductivity within the optimal dosage range of 5–10%, fully meeting the requirements for compressive strength (10.4–21.7 MPa) and fluidity (19.3–21.2 cm) of cementing. In addition, MEG-cement maintained stable density and significant high thermal conductivity advantage in high-mineralization environments (5–36% NaCl), with an increase in thermal conductivity of 23.8- 54.1%. 3) The mechanism of MEG promoting heat transfer in cement is summarized as the enhancement of the hydration process and the production of C-S-H gels. C-S-H gels filled the gel pores and transition pores in the cement skeleton and formed a dense, high thermal conductivity network, which shortens the heat transfer path and thus greatly improves the thermal conductivity of cement. In summary, this study has successfully developed a MEG geothermal cement with independent intellectual property rights that provides reliable technical support for the efficient development of geothermal resources and has important engineering application value.

Keywords Geothermal exploitation, Casing cement, Modified expanded graphite, Thermal conductivity enhancement, Thermal conductivity mechanism

Geothermal energy has garnered significant interest as a clean and renewable resource because of its low direct use costs, non-emission of greenhouse gases, and steady and continuous heat source. It is crucial to meet energy demand and accomplish the decarbonization revolution[1–5]. To harvest thermal energy, a geothermal well's goal is to reach the geothermal reservoir, generate geothermal fluids, and circulate them (see Fig. 1). Cementing is a crucial step in finishing geothermal wells, which establishes the production capacity, service life, and stability of wells during the entire life cycle of wells[6–8]. Researchers have improved the cement technology by creating a

[1]School of Civil Engineering and Architecture, Henan University, Henan 475004, People's Republic of China. [2]Key Laboratory of Shallow Geothermal Energy, Ministry of Natural Resources of the People's Republic of China, Beijing 100195, China. [3]State Key Laboratory of Geohazard Prevention and Geoenvironment Protection (SKLGP), Chengdu University of Technology, Chengdu, China. ✉email: zhuwenxidida@163.com

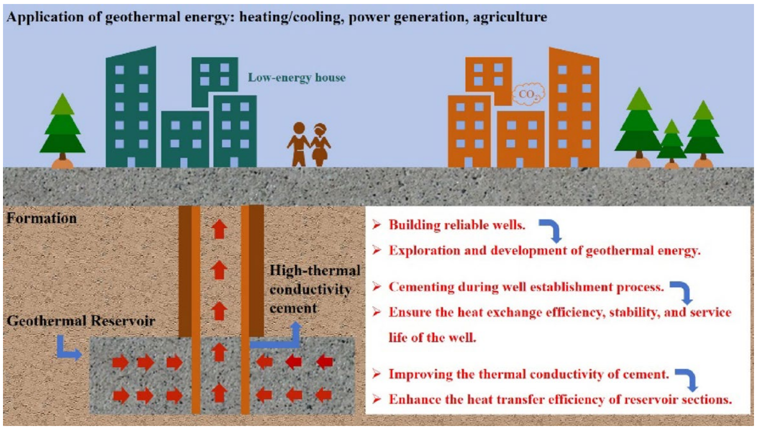

Fig. 1. Schematic diagram of geothermal energy well construction for heat extraction.

variety of geothermal cement systems that are high strength, corrosion-resistant, self-healing, and resistant to high temperatures[9–11].

The biggest challenge for efficient heat transfer and economic development of geothermal energy is the insufficient thermal conductivity of the existing cement system. The cement layer that sits between the casing and the reservoir makes direct contact with the geothermal reservoir and transfers heat to the casing through thermal conduction. Consequently, the primary heat transfer medium between the reservoir and the wellbore is cement. The geothermal well's exit temperature is directly influenced by its thermal conductivity[12]. According to some state-of-the-art numerical simulation results, the heat production power at 120 days increased by 10.29% when the cement's thermal conductivity was equal to that of the formation, suggesting that cement's thermal resistance plays a significant role in enhancing the heat generation effect[13]. In the mathematical and numerical models of thermal conductivity of cement-based composite materials (CBC), Yang et al. found that cubic fillers were more effective than spherical fillers in improving CBC thermal conductivity[14]. Han et al. suggested that thermal conductivity is the most significant element influencing the thermal recovery capacity of geothermal wells, aside from natural factors (well depth, geothermal gradient), based on the layered heat transfer model of medium/deep casing geothermal wells. When the cement's thermal conductivity rises from 0.4 W/(m·K) to 4.0 W/(m·K), the thermal power can increase by 29.4%, assuming the formation's thermal conductivity is 3.98 W/(m·K)[15].

Research on geothermal cement with high thermal conductivity has advanced rapidly in the past five years. Zhang et al. noted that the increase in porosity and hydration degree of cement particles can effectively reduce the heat transfer area and capacity of the skeleton, which is the primary factor affecting the thermal conductivity[16]. The favored option for cement fillers is carbon-based compounds due to their exceptionally high thermal conductivity. A network of heat conduction is formed when enough graphite particles aggregate, according to Wang et al.'s analysis of the thermal conductivity mechanism of graphite-based cement. There are many more phonons moving through the heat conduction network. On the other hand, the addition of graphite can impede the hydration reaction, resulting in micro defects during the cement's hardening phase, which will somewhat reduce its strength and heat conductivity[17]. Composite phase change materials (CPCMs) based on expanded graphite, paraffin, and graphite nanoplatelets were created to enhance thermal properties. Nevertheless, the substance decreased cement's 28-day compressive strength by as much as 86.4%[18]. Song et al. optimized the dosage of thermal conductive materials graphite (0.05 ~ 0.15), ferrum (0.05 ~ 0.20), and copper (0.05 ~ 0.50). Unacceptable in cementing engineering, the strength of 0.2 graphite-cement significantly reduced from ~ 60 MPa to < 10 MPa[19]. According to research by Li et al., carbon nanotubes (CNTs), silicon nitride (Si_3N_4), and natural flake graphite (GP) can all be employed as fillers to increase the thermal conductivity of cement, but they also reduce the fluidity to differing degrees. For instance, cement containing 0.6% GP or 0.6% CNTs had a fluidity of ~ 12 cm, which was below the pumpability requirements for geothermal cement[20]. According to Li et al., silicon sand successfully raise the thermal conductivity of GCPB (Gangue introduced paste backfill) without lowering its compressive strength. But a decrease in fluidity was brought on by too much silicon sand (> 0.5%)[21]. In conclusion, cement's thermal conductivity can be effectively increased by using materials with high thermal conductivity. There is still a discrepancy between the cement's thermal conductivity coefficient and its upper limit [> 3.0 W/(m·K)]. The harm that modern thermal conductive materials bring to the performance of geothermal cement far outweighs national standards. The effects of high temperatures and high mineralization fluids in geothermal reservoirs on the performance of thermal conductive cement are not covered in the literature, and the dearth of information makes it challenging to utilize.

To solve these issues, the design and preparation of a novel epoxy resin (EP)-expanded graphite (EG) composite (MEG) was motivated by polymer-based materials. EP was selected as the substrate in an effort to improve the cement's mechanical qualities[22–24]. The carbon atoms in graphite form covalent bonds with three adjacent carbon atoms through sp^2 hybridization, while lone pair electrons in the same plane form delocalized large π bonds, allowing graphite to transfer heat mainly through the free movement of lone pair electrons in the plane, supplemented by lattice vibration. Consequently, graphite shows a high thermal conductivity of 129

Sample	Na_2O	MgO	Al_2O_3	SiO_2	K_2O	CaO	Fe_2O_3	CO_2
G-cement	0.30	19.71%	2.69%	20.79%	0.60%	51.57%	4.34%	--
S95 slag	0.57%	15.57%	10.79%	29.44%	0.33%	32.89%	0.25%	10.15%

Table 1. XRF analysis of G-cement and S95 slag.

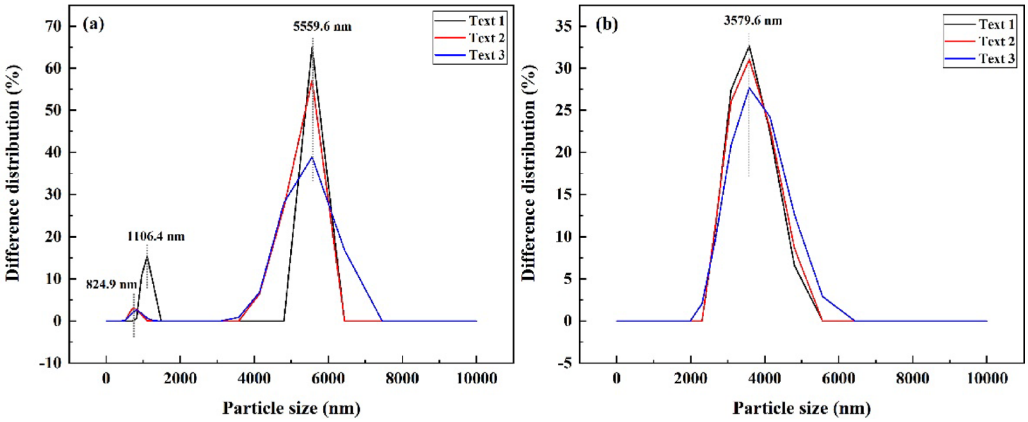

Fig. 2. Particle size distribution diagram of G-cement and S95 slag: (**a**) G-cement; (**b**) S95 slag.

W/(m·K)[25]. EG is produced by introducing the proper chemical reagents between graphite layers utilizing techniques such as chemical oxidation, microwaves, electrochemistry, and low-temperature/high-temperature thermal expansion[26]. As a result, EG is chosen as a high thermal conductivity filler because it maintains the benefits of natural graphite, including its high temperature resistance, corrosion resistance, and high thermal conductivity, in addition to its lightweight, compressible, and large specific surface area properties[27]. Zinc ion complex (ZDMA) is utilized as a bridge for MEG composites because of its curing impact on EP and the strong cation-π contact force between ZDMA and EG, i.e. the interaction between positively charged cations and negatively charged π electron clouds[28–31].

In response to the problems of mechanical performance degradation, insufficient flowability, and lack of adaptability to high temperature and high mineralization environments caused by the addition of fillers in existing high thermal conductivity geothermal cement, this study aims to design a novel epoxy resin/expanded graphite composite additive (MEG) that synergistically optimizes the thermal conductivity, mechanical properties, and engineering applicability of cement through the cation-π interface bridging mechanism. The focus is to explore how MEG can significantly improve the thermal conductivity while ensuring the compressive strength (≥ 10.3 MPa), liquidity (controlled at 17–24 cm), and high salinity stability in the geothermal cementing environment (60–100 ℃, 5–36% NaCl) by regulating the nucleation of C-S-H gel, pore filling, and thermal conductivity network construction. This study aims to break the bottleneck of traditional thermal conductive fillers with high thermal conductivity and low performance, and provide material basis and theoretical support for efficient thermal recovery of geothermal wells.

Materials and methods

Materials

The geothermal cement sheath has long been subjected to a high-temperature and high-mineralization fluid erosion environment. Based on previous research, a high sulfur-resistant G-grade cement (HSR G-cement) with temperature-resistant and corrosion-resistant was selected[32]. G-cement was purchased from Kangjing Building Materials Co., Ltd. S95 slag powder was purchased from Henan Dingnuo Purification Materials Co., Ltd and was prepared from blast furnace slag through drying, grinding, and other processes to improve the mechanical properties of cement. The main elemental components of G-cement and S95 slag were analyzed using X-ray Fluorescence spectrometer (XRF), as listed in Table 1. The particle size distribution of G-cement and S95 slag is shown in Fig. 2, with each sample tested 3 times. Results indicate that the particle size of G-cement is concentrated at 5559.6 nm, with a small amount distributed in 824.9 and 1106.4 nm. S95 slag is mainly composed of particles with a diameter of 3579.6 nm.

N-Hexane (AR 97%), nano zinc oxide (99.8%, 50 ±10 nm), and methacrylic acid (MMA, 98%) were purchased from Shanghai Aladdin Biochemical Technology Co., Ltd. Expanded graphite (EG, 325 mush, 99.9%) with 450 ml/g original expansion volume was purchased from Suqian Nakaite New Materials Technology Co., Ltd. Low viscosity epoxy resin (EP) was purchased from Kunshan Jiulimei Electronic Materials Co., Ltd. The epoxy value of EP is 0.54–0.6 equivalents/100 g and the viscosity at 25 ℃ is 800–1200 mPa·s.

Method

Preparation of modified expanded graphite (MEG)

Figure 3 depicts the MEG preparation procedure. First, nano zinc oxide (0.55 g) and methacrylic acid (1.21 g) were added to a beaker with 50 mL of N-hexane. The mixture was then stirred at room temperature for 30 min to obtain a white zinc ion complex ZDMA. Add EG (5.4 g) and EP (10.96 g) to ZDMA in sequence, while adding sufficient N-hexane to ensure uniform dispersion of the above materials. After continuous heating and stirring at 80 ℃ for 2 h, modified expanded graphite (MEG) can be obtained by volatilizing N-hexane. It is important to note that the volatile N-hexane can be recycled and reused in industrial production.

Preparation and performance testing of cement

The preparation and performance testing of cement refer to "GB/T 19139 – 2012" and "SY/T 5546-92". In the pre-experiment, the influence of the cement/slag ratio (9:1/8:2/7:3/6:4/5:5) and a water cement ratio (0.4/0.5/0.6/0.7) on the performance of cement properties was analyzed. The basic formula that meets the geothermal cementing requirements and has the highest compressive strength was selected as the control group: cement-S95 slag ratio of 6:4 and a water-cement ratio (w/c ratio) of 0.6. Mix dry materials (G cement, S95 slag, and MEG) at low speed for 2 min, and then pour the mixture into a low-speed stirred water-containing slurry mixer (Model NJ-160B, China) to prepare cement slurry. Make sure to record the cement fluidity using the truncated cone method immediately. Then pour the cement slurry into a triple cube mold (40 × 40 × 40 mm) and a disc-shaped mold (diameter 130 mm, thickness 10 mm), and cure at 60/80/100 ℃ for 72 h.

The literature reports serve as the basis for determining the curing temperature. Geothermal well drilling typically has an average temperature of 85 °C because of the cooling imp-act of the drilling fluid[33,34]. As reported, the bottom hole circulation temperature (BHCT) corresponding to a formation temperature of 183.29 ℃ is only 98.2 ℃[35]. The BHCT of the Los Azufres oil field well in Mexico was 83 ℃ after the well was shut in (with a formation temperature of 116 ℃)[36]. Even if the formation temperature is 350 ℃, drilling fluid can still be cooled appropriately based on the cooling system to maintain the BHCT at about 80 ℃[37]. To cover the bottom hole temperature of the great majority of geothermal wells, this study set the curing temperature between 60 and 100 °C.

Microcomputer-controlled electronic universal testing machine (Model WDW-600E, China) was used to characterize the compressive strength of square cement test blocks. Take the average of three tests per group.

The thermal conductivity of disc-shaped cement is tested using the DRP-II thermal conductivity tester, which is based on the flat plate steady-state method. After stable heat transfer, note the temperature of the heat-dissipating copper plate and compute the thermal conductivity using analysis software. The measurement precision is ±1 °C, the measuring range is 0.1~300 W/(m·K) at the room temperature ~ 110 °C.

Characterization of materials and analysis of thermal conductivity mechanism

Fourier transform infrared spectroscopy test (FT-IR) The Fourier transform infrared spectrometer (Model Bruker Tensor II, Germany) was used to test the FT-IR absorption spectra of solid samples at 4000 ~ 400 cm^{-1}.

UV visible absorption spectroscopy test (UV-vis) A small amount of EG, ZDMA, and MEG were mixed into a deep eutectic solvent and sonicated for 30 min. Take about 10 mL of solvent and composite fluids respectively, and pour into a capped cuvette. A UV visible absorption spectrometer (Model Cary 5000, Malaysia) was used to test the UV absorption spectrum in the range of 215–500 nm.

Scanning electron microscope (SEM) and energy spectrum analysis (EDS) A field emission scanning electron microscopy system (Model JEOL JSM-7610 F Plus, Japan) was used to observe the microstructure of the sample. Meanwhile, the mapping images of the samples were scanned and the elemental composition and content were analyzed.

Thermal analysis test (TGA) A differential thermal thermogravimetric analyzer (Model TGA/DSC3+, Switzerland) was used to investigate the thermal stability of EG and MEG in a nitrogen atmosphere at a heating rate of 10 °C/min with a testing temperature range of 25–800 °C.

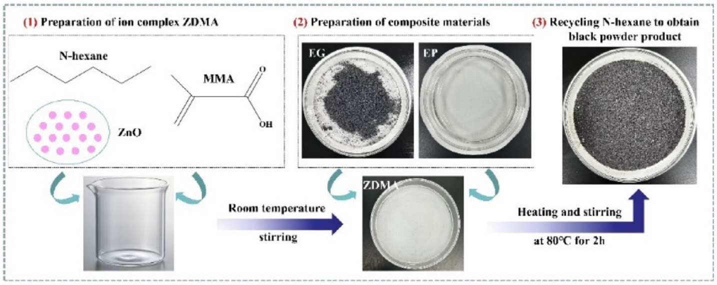

Fig. 3. Preparation schematic diagram of MEG.

X-ray diffraction analysis (XRD) Mineral analysis of cement powder samples was conducted using an X-ray diffraction analyzer (Model D8-ADVANCE, Germany). The 2θ angle was from 3° to 70° and the scan speed was 4 °/min.

Mercury intrusion porosimetry (MIP) Mercury intrusion porosimetry (Model PoreMaster-33, America) was used to test the porosity and pore size distribution of cement test blocks (approximately 0.5 cm in diameter).

Results and discussion

Characterization of MEG

FT-IR and UV-vis

Figure 4(a) shows the FT-IR of ZnO and ZDMA. The absorption peak at 436 cm^{-1} is a characteristic peak of nano ZnO, attributed to the stretching vibration of Zn-O. The peaks at 3422 cm^{-1}, 1631 cm^{-1}, and 1388 cm^{-1} represent the stretching vibration, bending vibration, and surface bridging vibration of hydroxyl groups, respectively[38]. After the reaction between MMA and ZnO, the hydrogen on the hydroxyl group in MMA is replaced by Zn^{2+}, and ZDMA does not contain the dimer -OH. Therefore, in the ZDMA spectrum, there is no strong and wide peak (3200 ~ 2500 cm^{-1}) generated by the stretching vibration of -OH. There were no coupling double peaks at 1431 cm^{-1} and 1299 cm^{-1}, which were generated by the bending vibration of - OH and the stretching vibration of -C-O, as well as the swinging vibration peak at ~ 920 cm^{-1} of the -OH[39]. Besides, in the ZDMA spectrum, the appearance of carbonyl double peaks at 1561 cm^{-1} and 1425 cm^{-1} indicated that the carboxylic acid group of MMA has been transformed into carboxylate[40], while the characteristic peak at 442 cm^{-1} indicates the presence of ZnO, which proves the synthesis of ZDMA.

As shown in Fig. 4 (b), to investigate the curing effect of synthesized ZDMA on epoxy resin (EP), FT-IR characterization was performed on the cured EP. The characteristic peak of ester group (-COOR) appeared at 1718 cm^{-1} in the spectrum, indicating the ring opening reaction between ZDMA and EP as shown in Fig. 5[41]. The presence of Zn^{2+} promote the ring opening reaction of EP. One end of ZDMA reacts with carboxylate groups to form ester bonds, while the other end combines with Zn^{2+} to promote ring opening. Finally, EP undergoes

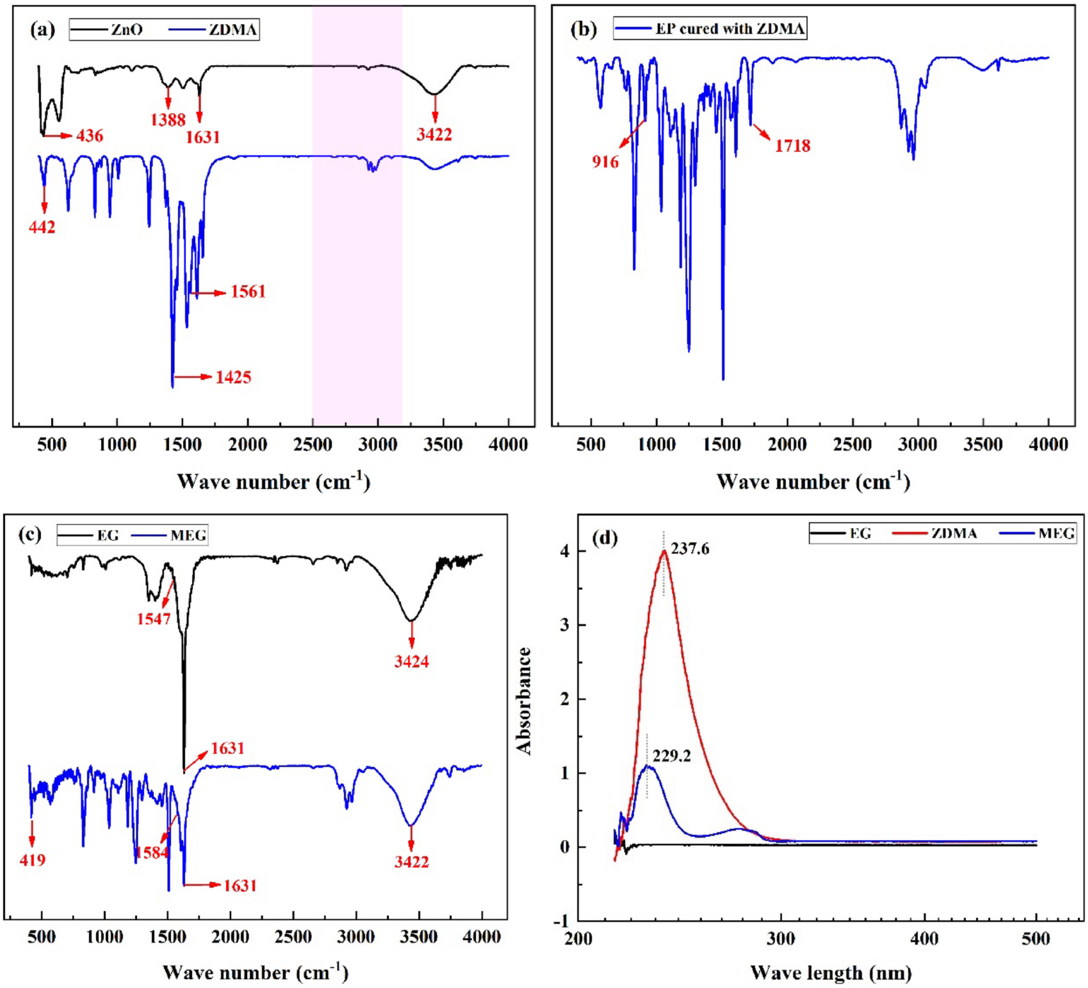

Fig. 4. FT-IR and UV-vis images: (**a**) FT-IR spectrum of ZnO and ZDMA; (**b**) FT-IR spectrum of EP; (**c**) FT-IR spectrum of EG and MEG; (**d**) UV-vis spectrum of ZDMA, EG, and MEG.

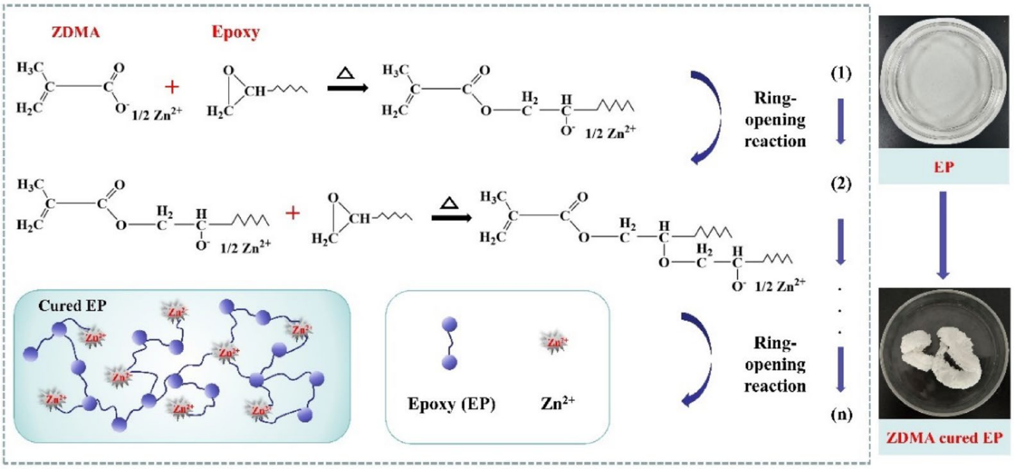

Fig. 5. Schematic diagram of the ring-opening reaction of ZDMA cured EP.

cross-linking and curing. It's worth noting that the characteristic absorption peak of the epoxy group at 916 cm^{-1} has not disappeared, indicating that there is still an unopened EP residue.

Figure 4(c) shows the FT-IR of EG and MEG. The absorption peak at 3424 cm^{-1} is attributed to the stretching vibration of -OH in the interlayer adsorbed water of graphite. The peak at 1631 cm^{-1} and 1547 cm^{-1} characterized the stretching vibration of C = C in the benzene ring structure of graphite crystal. MEG contains characteristic peaks of both EG and ZDMA, which preliminarily proves the composite effect of Zn^{2+} and EG[42]. To confirm the presence of cation-π interaction in the system, UV visible absorption spectroscopy (UV-vis) was applied to characterize the ZDMA, EG, and MEG samples, as shown in Fig. 4(d). ZDMA shows an absorption band at 220–280 nm, while EG has no significant absorption peak in the wavelength range of 215–500 nm. In the spectrum of ZDMA loaded with EG (i.e. MEG), the absorption peak redshifts from 237.6 nm to 229.2 nm, indicating that there is indeed cation-π interaction between Zn^{2+} in ZDMA and EG[43].

In summary, the products and synthesis principles of each reaction stage were characterized by FTIR and UV-Vis tests, and based on this, the chemical reaction structural formula in Fig. 5 was obtained. The accuracy of the design principle was demonstrated: the zinc ion complex ZDMA participates in the ring-opening reaction of EP and cures it. ZDMA also forms a complex with EG through the strong cation-π bond bridging principle. These provide a basis for the filling design of new porous media.

SEM

The SEM and EDS analysis of EG and MEG are shown in Figs. 6 and 7, respectively. An essential structure and basis for EG's application as a loading matrix material is the honeycomb-like connected network structure, which is made up of nanographite layers at the microscopic level (Fig. 6(a$_{1-3}$))[44,45]. This continuous three-dimensional network structure is connected by van der Waals forces between graphite sheets of nanoscale thickness. This can lower interfacial thermal resistance between graphite, lessen phonon scattering between graphite sheets, and offer a superior heat transmission pathway[46].

Figure 6(b$_{1-3}$) shows the morphology of MEG at different magnifications. At a high magnification of ×5000, the surface of MEG is smooth and flat, and the honeycomb-like pore structure on the EG surface is filled. Figures 7(a$_{1-2}$) and 7(b$_{1-2}$) show that the EDS mapping of the C element is consistent with the morphology of EG and MEG, with carbon being the main component of EG and MEG. Differently, it can be observed that zinc comes from ZDMA and is uniformly dispersed on the surface of MEG, further proving the link between MEG and ZDMA. Therefore, SEM further confirms the bonding effect of ADMA and the effective filling of the EG honeycomb structure by EP. The dense structure will further assist EG in constructing a high thermal conductivity path and exerting its thermal conductivity enhancement effect.

TGA

The engineering uses of materials in high-temperature geothermal systems are correlated with their thermal stability. Figure 8 displays the thermal weight loss properties of MEG and EG. With a low decomposition rate (≤ −0.107%/min), the mass loss of EG from thermal decomposition is only 4.34% within the testing range of ambient temperature to 800 °C. Therefore, EG barely breaks down in a geothermal reservoir setting due to its extraordinarily high thermal breakdown temperature.

Under the same heating rate, MEG exhibited a completely different thermogravimetric curve. Three stages may be distinguished in the decomposition of MEG: a mass loss of 7.03% is generated at room temperature (~300℃), which is mainly attributed to the decomposition of EP outside EG directly in contact with the gas. The decomposition rate in this stage is relatively low (≤ −0.078%/min); The main decomposition of MEG occurs in the range of 300–500 ℃, with a 41.17% mass loss. It has the highest decomposition rate at 366 ℃, which is −0.74%/min, corresponding to the decomposition of EP in EG micropores; The thermal decomposition of cured

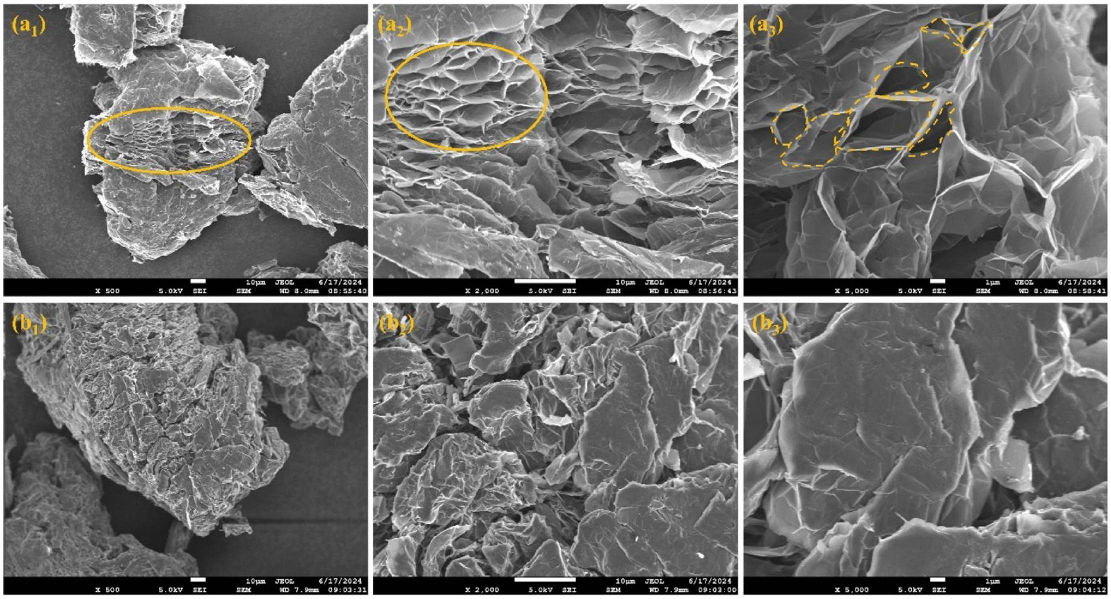

Fig. 6. SEM images of sample: (**a**$_{1-3}$) morphological image of EG at ×500, ×2000, ×5000, respectively; (**b**$_{1-3}$) morphological image of MEG at ×500, ×2000, ×5000, respectively.

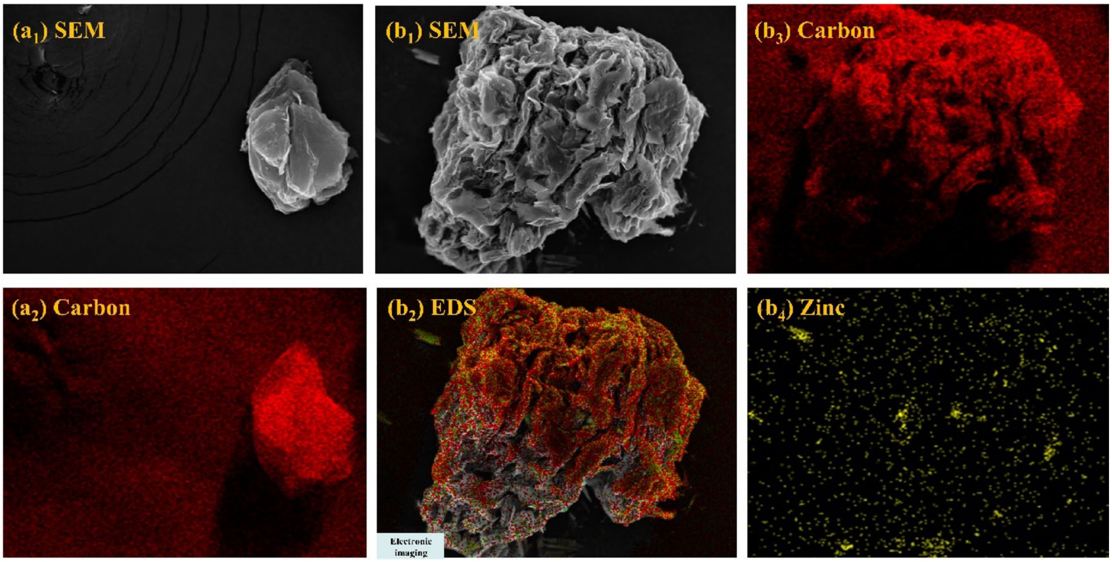

Fig. 7. EDS and mapping images of samples: (**a**$_{1-2}$) SEM and mapping images of EG; (**b**$_{1-4}$) SEM, EDS layered image, and mapping images of MEG.

EP usually ends at about > 500 ℃[47]. Therefore, the decomposition rate of MEG tends to be flat at 500–800 ℃. At this temperature, the decomposition of raw material EG mainly occurs, with a mass loss of 3.05%.

In conclusion, the thermal decomposition temperature of EG was lowered by the addition of ZDMA and EP. Nevertheless, MEG maintains a heat loss of less than 1.12% and possesses thermal stability that satisfies geothermal cementing requirements in the hydrothermal geothermal reservoir environment (< 150 °C).

The thermal conductivity evaluation of cement

Testing for thermal conductivity provides a clear and accurate picture of cement materials' capacity for heat transfer, as depicted in Fig. 9. The thermal conductivity of G-cement (control group) started to rise dramatically at various MEG dosages (2.5–15%), increasing by 20.7–182.1%. MEG is the primary component in enhancing the thermal conductivity of composite materials because of its high thermal conductivity and large specific surface area, which encourages the development of a heat transfer network. Table 2 further illustrates the notable

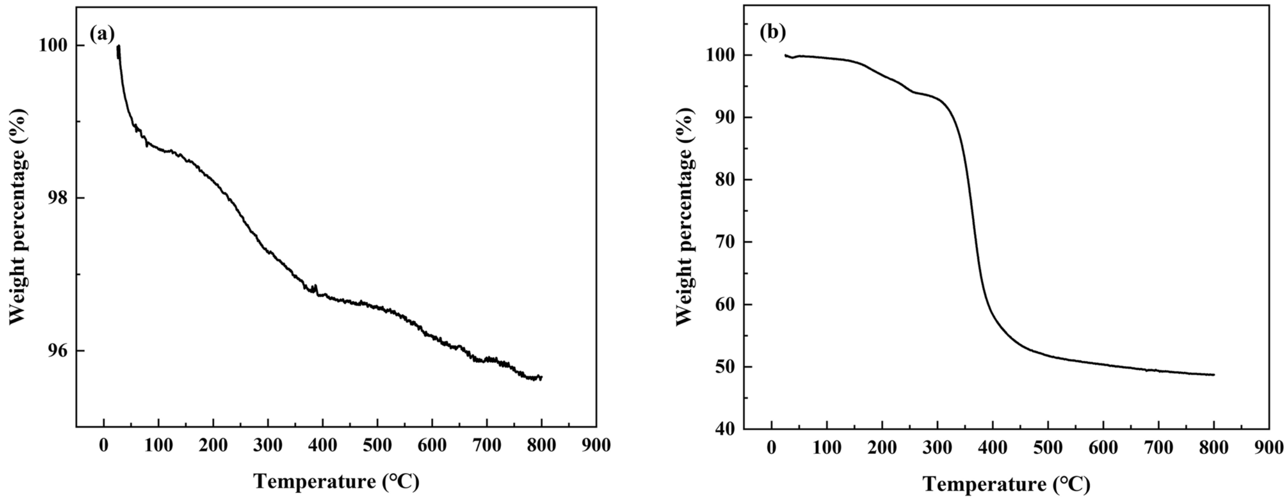

Fig. 8. TGA curves of EG and MEG: (**a**) EG; (**b**) MEG.

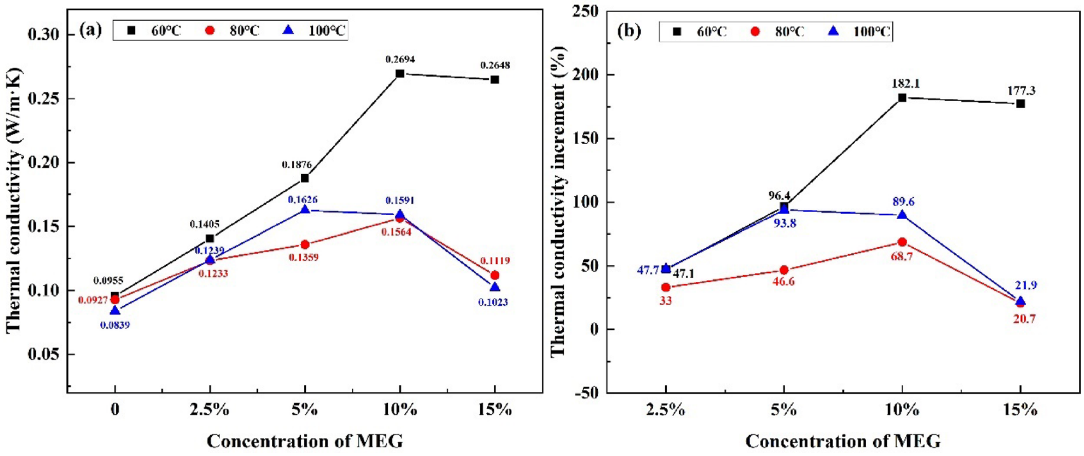

Fig. 9. Thermal conductivity of G cement and MEG-cement at different temperatures: (**a**) thermal conductivity; (**b**) thermal conductivity increment.

No and Ref	Thermal conductive materials	Thermal conductivity increment
1	MEG	20.7–182.1%
2[49]	Iron powder	24.7%
	Graphite (325 mesh)	15.5%
	Silicon carbide	15.0%
	Carbon fiber	34.9%
3[50]	10% $ScCO_2$ modified ground-granulated blast furnace slag	23.3%
4[25]	Graphite: alumina: steel slag = 1:2:1	25.3%
	Graphite: alumina: steel slag = 1:3:3	41.8%

Table 2. Comparison of the thermal conductivity increment of cement by different high-thermal conductive materials.

enhancement of MEG on the thermal conductivity of cement by showing that its synergistic effect is significantly larger than that of other types of thermal conductive fillers produced in recent years (15–41.8%).

The dosage and curing temperature of MEG have a considerable impact on its enhancing effect. The thermal conductivity of 2.5% MEG cement at 60 °C is 0.1405 W/(m·K), 51.6% higher than that of the MEG-free control group (0.0955 W/(m·K)), demonstrating a notable improvement of thermal conductivity. As MEG concentration rises, cement's thermal conductivity and thermal conductivity increment exhibit a trend of first rising and then falling. The thermal conductivity rose to 0.2694 W/(m·K) and then gradually dropped to 0.2648 W/(m·K) as the MEG content was steadily raised to 15%. Despite this, the thermal conductivity of 15% MEG-cement was still 177.3% greater than that of the control group. This occurrence suggests that a thermal conduction channel network can be efficiently formed with low-dose MEG, and that the production of thermal conduction pathway networks peaks at 10% MEG. Cracks may form and interfacial thermal resistance may rise as a result of uneven volume changes between the filler and cement during agglomeration or solidification caused by excessive addition[48].

The pattern of MEG cement at 80 °C and 100 °C is consistent with that at 60 °C. After curing at 80 and 100 ℃, the thermal conductivity reached peak values of 0.1564 W/(m·K) and 0.1626 W/(m·K) at 10% and 5% MEG content, respectively, which increased by 68.7% and 93.8% compared to the control group. The findings show that cement's thermal conductivity may be greatly increased (46.6–182.1%) by carefully regulating the amount of MEG (5–10%) and matching the curing temperature. This provides a solid foundation for effective heat transfer in geothermal wells.

The compressive strength, density, and fluidity properties of cement

The multi-objective optimization law of geothermal cementing was discovered by creating a relationship curve between the following parameters: MEG concentration (2.5–15%), curing temperature (60–100 °C), and material qualities (compressive strength, flowability, and density). Results show that the new developed MEG-cement fully meets the requirements of geothermal cementing engineering and exhibits unique advantages.

As shown in Fig. 10 (a), through the nucleation effect, 2.5% MEG raised the bulk density of the C-S-H gel at 60 °C and enhanced the compressive strength (CS) to 24.8 MPa (6.9% higher than the control group). The CS value tends to first rise and then fall with increasing MEG concentration. This is mostly due to changes in the distribution of pore sizes and an increase in the percentage of 0.1–1 μm capillary pores. However, the strength is stabilized around 10.4–21.7 MPa due to the strong bonding of 5–10%MEG molecules at the cement transition contact, completely meeting the API standard requirements. It is noteworthy that even at a high temperature of 100 °C, the system retains a benchmark strength of ≥ 10.6 MPa.

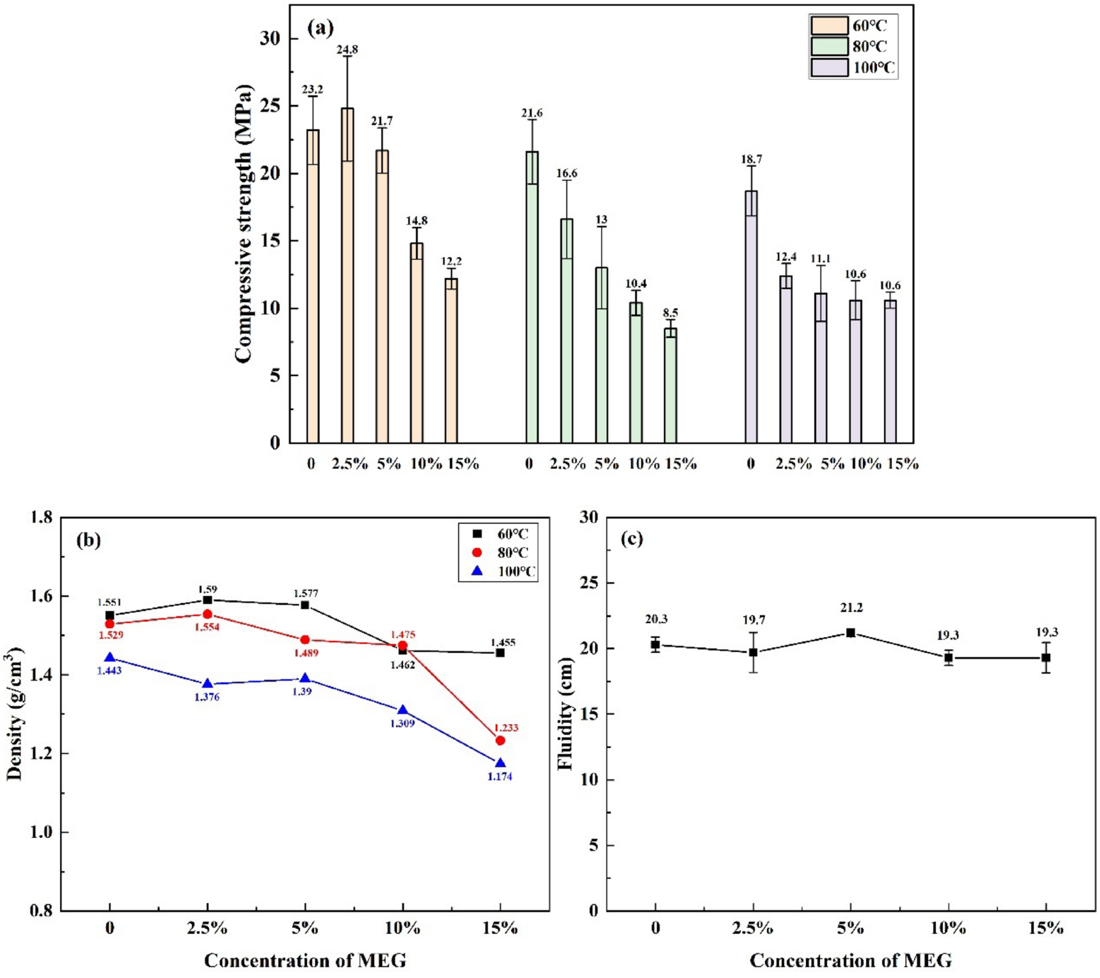

Fig. 10. Basic performance evaluation of MEG-cement cured at different temperatures: (**a**) compressive strength; (**b**) density; (**c**) fluidity.

Through a dynamic hydrogen bonding network, the filler material EP in MEG can create a steric hindrance effect that effectively suppresses the cement particles' propensity to flocculate, forms a lubricating layer, and ensures the fluidity of the cement slurry. The outstanding pumpability of MEG cement is demonstrated by the construction performance evaluation (Fig. 10(b)). The on-site construction requirements are met by the stable flowability, which ranges from 19.3 to 21.2 cm with a fluctuation amplitude of less than 5%, within the dosage range of 2.5–15%. Under challenging geothermal well circumstances, this characteristic guarantees efficient pumping and wellbore stability of MEG cement.

According to the results of the density test (Fig. 10 (c)), MEG-cement offers notable benefits in terms of density management. The densities at 60/80/100 °C curing conditions are 1.462–1.577, 1.475–1.489, and 1.309–1.39 g/cm^3, respectively, within the optimum dose range. These densities are roughly 6–19% lower than traditional cement. Given that geothermal resources are primarily found in low-pressure rocks with developed pores and cracks, this feature matches the characteristics of geothermal reservoirs[51]. A lower density can successfully lower the cement slurry column's pressure, lower the chance of leaks, and enhance cementing quality.

In summary, MEG-cement has achieved a breakthrough in synergistic enhancement of thermal conductivity, mechanical properties, construction performance, and reservoir adaptability, providing a low-cost cement solution for efficient heat transfer in geothermal wells. Its unique density adjustability is particularly suitable for low-pressure and leaky geothermal reservoirs and has broad engineering application prospects.

Evaluation of salt ion pollution resistance

A 5–36% NaCl gradient concentration salt solution was created to replicate the reservoir brine environment using the hydro-chemical database of common geothermal fields, such as the North China Basin in China[52–54]. The regulatory law of salinity on the characteristics of MEG-cement was covered. Results are shown in Fig. 11. As the fluidity test of cement was conducted before solidification, it is not discussed.

Micro-sized MEG particles are less affected by salt ions and construct a continuous thermal conductivity network by filling capillary pores. The micro expansion characteristics of MEG can also compensate for the volume shrinkage caused by salt crystallization and protect the thermal conductivity channel structure. Figure 11 (a) illustrates that MEG-cement consistently outperforms G-cement in terms of thermal conductivity, giving it a notable edge under high mineralization fluid circumstances. In a 5/10/15/20/25/30/36% NaCl environment, the thermal conductivity of MEG-cement increased by 23.8%, 34.0%, 37.8%, 32.9%, 42.1%, 54.1%, and 45.2%,

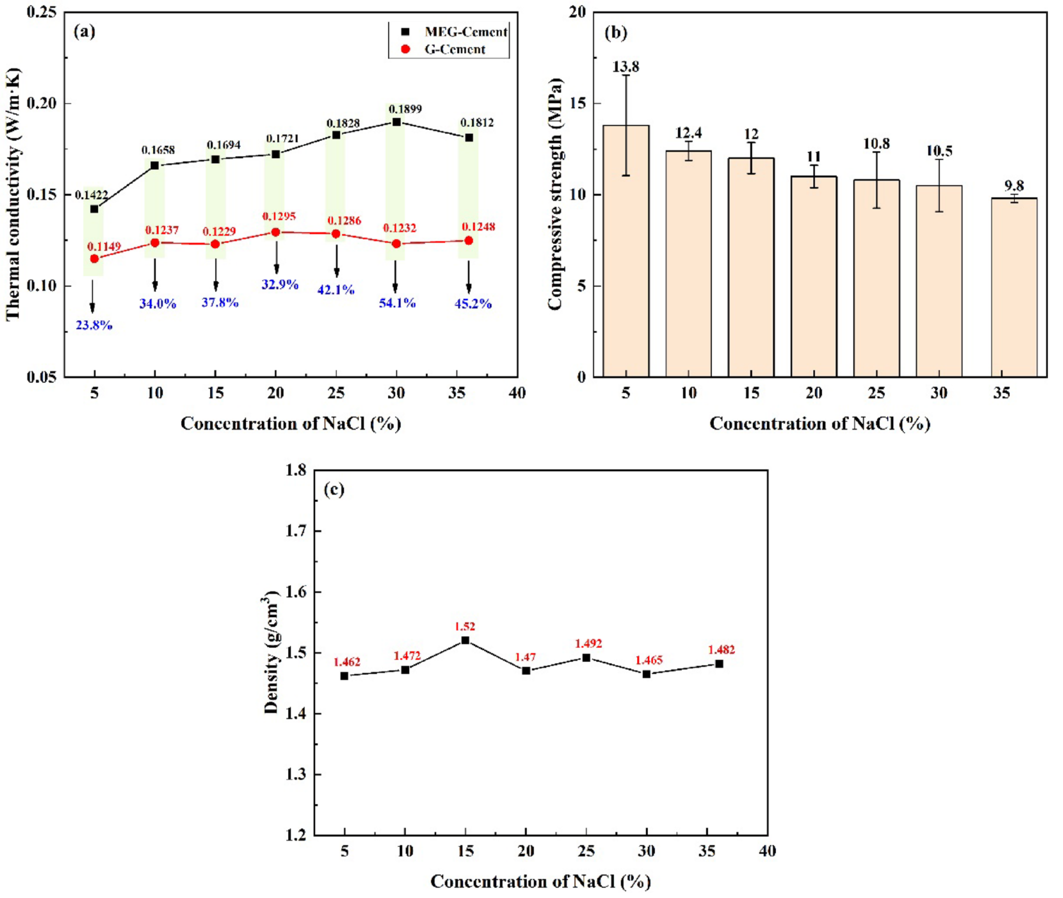

Fig. 11. Properties of G-cement and MEG-cement cured with different concentrations of NaCl solutions: (**a**) thermal conductivity; (**b**) compressive strength; (**c**) density.

respectively, in comparison to G-cement. Wang et al.‘s research has pointed out that when the content of NaCl is high, it will inhibit the early hydration rate of cement, promoting a significant increase in the proportion of harmful pores and a decrease in cement strength. This phenomenon may be particularly significant in high salinity geothermal environments[55]. However, as shown in Fig. 11 (b), the effect of NaCl on the CS of MEG-cement was minimal in contrast to the 10% MEG-cement cured with fresh water (14.8 MPa). When the concentration of NaCl increased from 5% to saturation, the CS value of MEG-cement fluctuated between 9.8 and 13.8 MPa, and the reduction rate was within 35%. Although NaCl has a slight detrimental impact on the strength of MEG-cement, with suitable material design, MEG-cement is still projected to display outstanding adaptability in high-salinity geothermal situations. In high mineralization settings, it is advised to include additives like nano silica[56], rutin[57], and fiber materials[58] to further improve the mechanical qualities of MEG-cement[59]. According to experiments, CS of cement can be increased by roughly 58.9% by adding 3% nano-silica. Furthermore, the use of fiber elements can increase cement’s durability by at least 30%.

As shown in Fig. 11 (c), with the increase in NaCl concentration, the density of MEG cement fluctuates between 1.462 and 1.520 g/cm^3. Compared with MEG cement cured in clean water, the addition of NaCl slightly increased the density of the cement, but the change remained within an acceptable range (< 4%). This result indicates that MEG cement can still maintain good density stability in high-salinity environments, which is crucial for achieving formation stability in high-pressure and high-salinity geothermal reservoirs. The small range of density variation of MEG cement further proves its reliability in practical geothermal engineering. Achieving formation stability in high-pressure and high-salinity geothermal reservoirs requires that MEG cement be able to retain strong density stability in high-salinity conditions, as this research shows. The narrow density variation of MEG cement further demonstrates its dependability in geothermal engineering applications.

Analysis of thermal conductivity mechanism of MEG-Cement

XRD

The different crystal phases found in G-cement and MEG-cement cured at 60/80/100°C were examined by XRD analysis, as seen in Figs. 12(a), (b), and (c), respectively. In the XRD curves of the control group, the peak at 2θ of ~ 12° belongs to un-hydrated C_4AF[60]. While in MEG-cement, the characteristic peaks of ZDMA and C_4AF overlap at ~ 12°. The peaks belonging to ettringite (AFt) appeared at 2θ of ~ 15°. The peaks at 2θ of ~ 29°, ~ 32°, ~ 41° relate to un-hydrated C_2S and C_3S[61]. $CaCO_3$ showed peaks at 2θ of ~ 23°.The peaks related to $Ca(OH)_2$ were identified at 2θ of ~ 18°, 34°, 47°, 50°, and 54°[62]. Due to the addition of ZDMA and EG, MEG-cement showed some unusually strong peaks at 2θ of about 12° when compared to the control group. New peaks appeared at 2θ

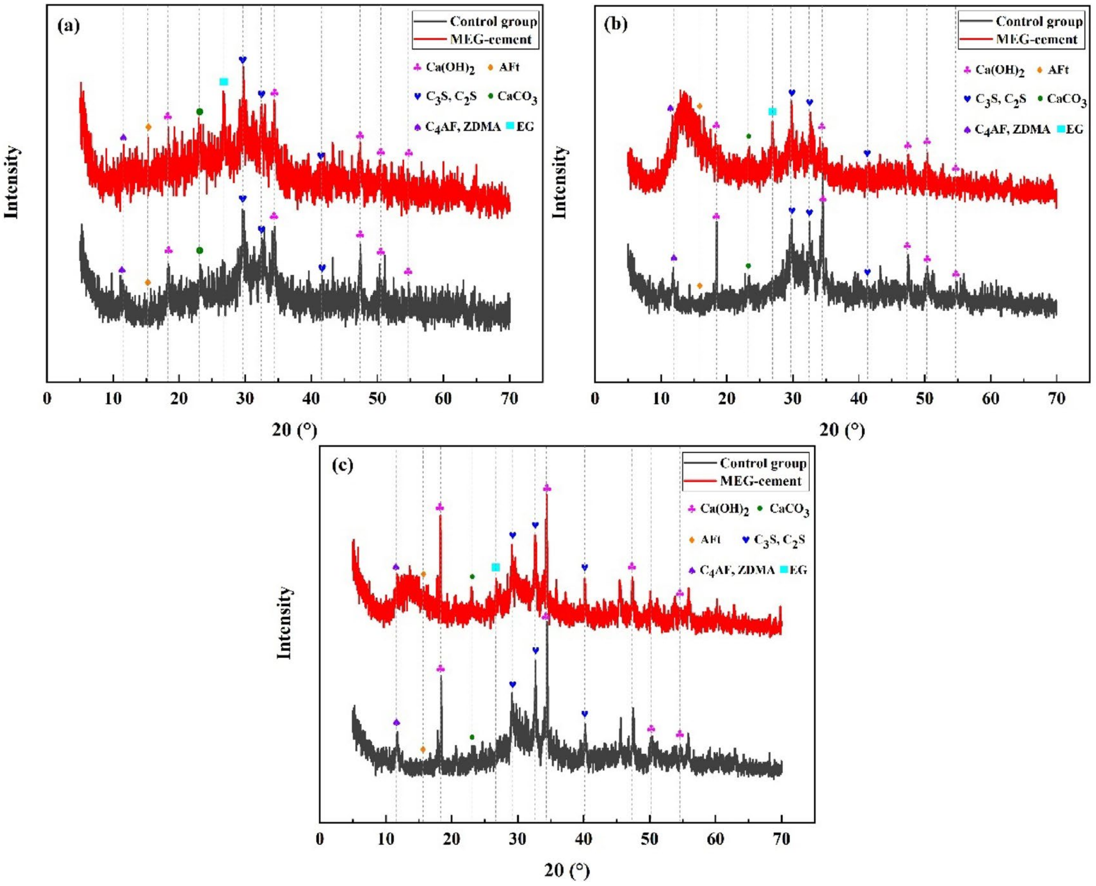

Fig. 12. XRD of cement samples at different curing conditions: (**a**) 60 ℃; (**b**) 80 ℃; (**c**) 100 ℃.

of ~ 26°, corresponding to EG. In addition, MEG-cement exhibited the same hydration products as G-cement, mainly including C-S-H gel, un-hydrated C_2S and C_3S, Ca $(OH)_2$, AFt, etc., suggesting that the addition of MEG did not result in the formation of extra crystal hydration products.

FT-IR

FTIR analysis is used to reveal the molecular level regulatory mechanism of MEG on the hydration kinetics of G-cement, as shown in Fig. 13(a), (b), and (c). The $Ca(OH)_2$ exhibited a sharp peak at 3620 ~ 3640 cm^{-1}. The -O-H in water molecules and C-S-H showed as a broad absorption in the range of 3000 ~ 3800 cm^{-1}. The bending vibration of H-O-H (v2) showed a characteristic peak at ~ 1650 cm^{-1}. In sulfates and ettringite, the vibration of SO_4^{2-} showed a peak at ~ 1110 cm^{-1}. The asymmetric stretching and out-of-plane bending of CO_3^{2-} corresponded to a broad range at about 1410 ~ 1480 cm^{-1} and 873 cm^{-1}, respectively. The presence of $CaCO_3$ was attributed to the atmospheric CO_2 absorbed during the air hydration sample. The strong bands at ~ 970 cm^{-1} were assigned to the Si-O or Al-O in C-S-H. The in-plane and out-of-plane Si-O bending vibrations of C-S-H appeared at ~ 450 cm^{-1} and ~ 520 cm^{-1}, respectively[62–65]. MEG-cement's FT-IR spectra in Fig. 13 (a-c) were comparable to those of the control group, suggesting the lack of novel hydration products.

The amount of C-S-H in hydration products was quantitatively analyzed using the most visible vibration absorption peak at approximately 970 cm^{-1}, as indicated in Table 3. Obviously, the peak intensity and integral area of MEG-cement cured at 60/80/100 ℃ were 53.3%, 155.5%, 466.2% higher than those of the G-cement, respectively. In addition, the absorption peaks of C_3S and C_2S, which are mainly characterized by Si-O bond vibrations, are reflected at the low wavenumber range of ~ 920 cm^{-1}. As the polymerization of the silicon-oxide tetrahedron, the Si-O vibration absorption peaks gradually migrate towards the high wavenumber range of ~ 980 cm^{-1}[64,66]. In Fig. 13 (a), (b), and (c), the characteristic peak shifts from 964 cm^{-1} (G-cement) to 966 cm^{-1} (MEG moment), from 957 cm^{-1} to 963 cm^{-1}, and from 949 cm^{-1} to 963 cm^{-1}, respectively. This means a decrease in un-hydrated C_2S/C_3S and a corresponding increase in C-S-H. In summary, it was demonstrated that the addition of MEG accelerated the cement's hydration process and the development of C-S-H gel in the hydration products.

SEM

The optimization process of MEG on the microstructure of cement-based materials was methodically disclosed by SEM technology (Fig. 14). The spatial distribution of G-cement's hydration products at 60–100℃ exhibited notable heterogeneity, according to the micro-morphological investigation (Fig. 14a_1-c_1). Clustered C-S-H gel

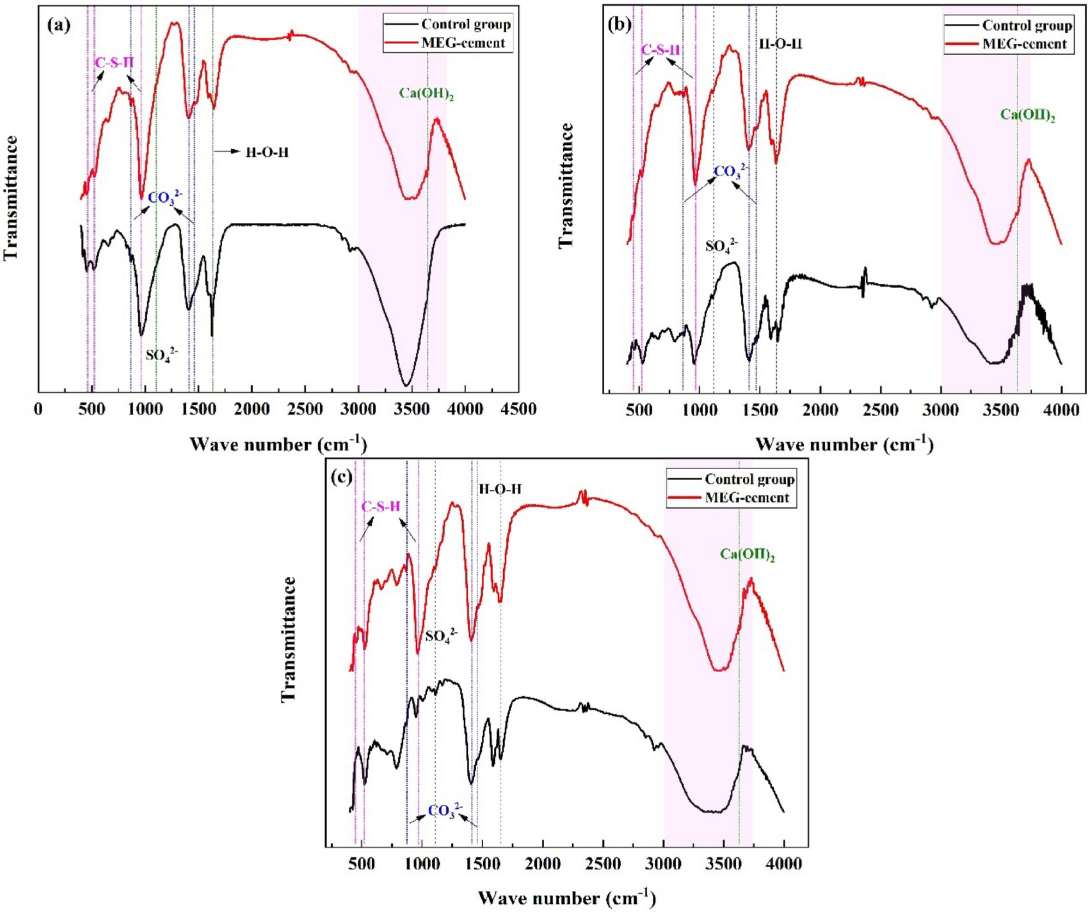

Fig. 13. FT-IR spectrum of cement samples at different curing conditions: (**a**) 60 ℃; (**b**) 80 ℃; (**c**) 100 ℃.

Curing condition	Sample	Peak	Integral area
60 ℃	G-cement	$964\ cm^{-1}$	25.233
	MEG-cement	$966\ cm^{-1}$	38.691
80 ℃	G-cement	$957\ cm^{-1}$	17.145
	MEG-cement	$963\ cm^{-1}$	43.801
100 ℃	G-cement	$949\ cm^{-1}$	4.600
	MEG-cement	$963\ cm^{-1}$	26.045

Table 3. The intensity and peak area of C-S-H characteristic peaks (~ 970 cm^{-1}).

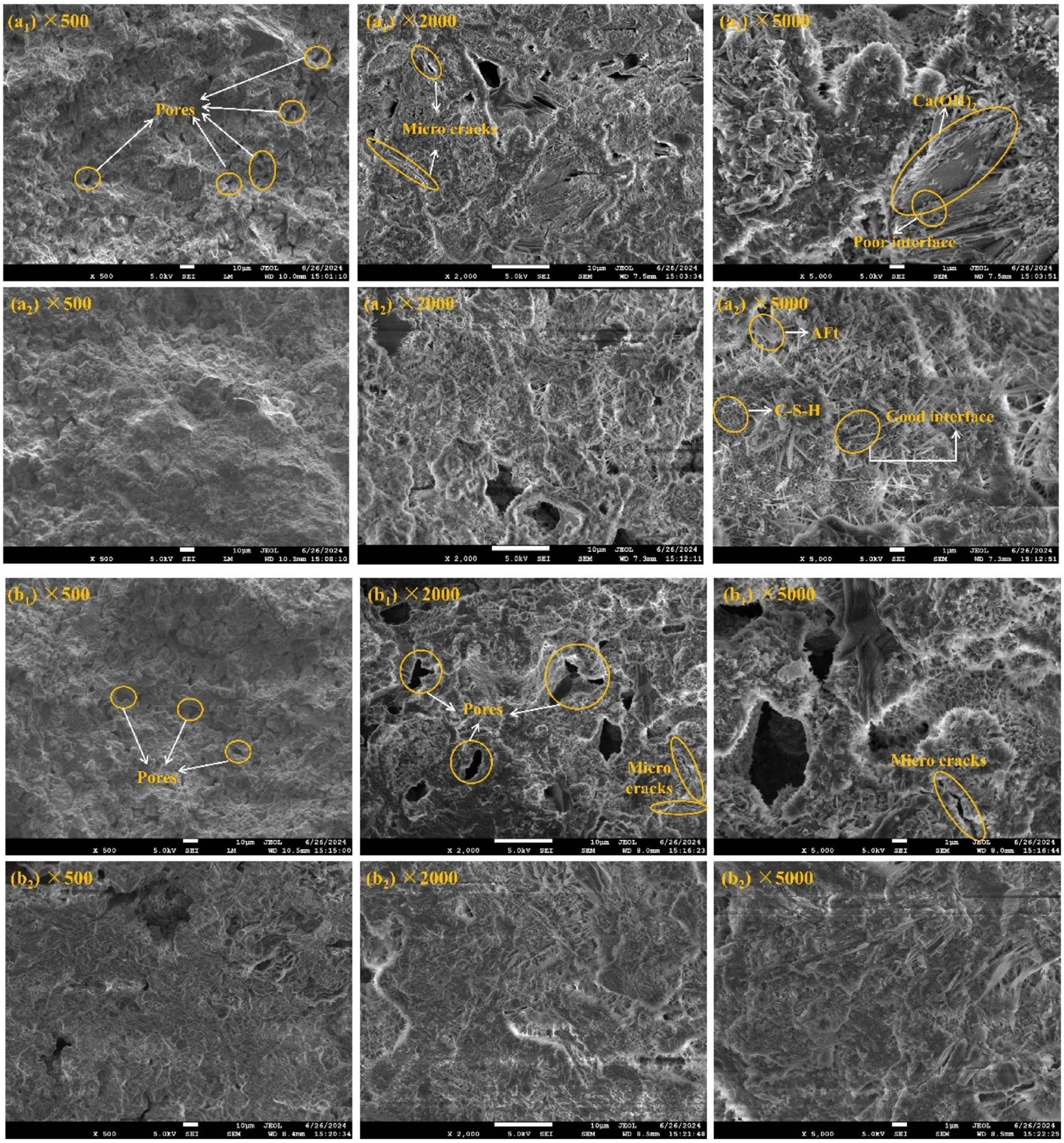

Fig. 14. SEM of cement samples at different curing conditions: (**a_1**) 60 ℃, G-cement; (a_2) 60 ℃, MEG-cement; (**b_1**) 80 ℃, G-cement; (**b_2**) 80 ℃, MEG-cement, position 1; (**b_3**) 80 ℃, MEG-cement, position 2; (**c_1**) 100 ℃, G-cement; (**c_2**) 100 ℃, MEG-cement.

and acicular ettringite (AFt) present discrete distribution characteristics[67–69]. The disordered stacking of plate-like Ca (OH) $_2$ crystals forms micro-scale pores (5–10 μ m), particularly where there is a clear phase separation at the aggregate-slurry interface transition zone. This results in loose structure and high porosity in the region, interrupting the effective thermal conductivity path of the matrix.

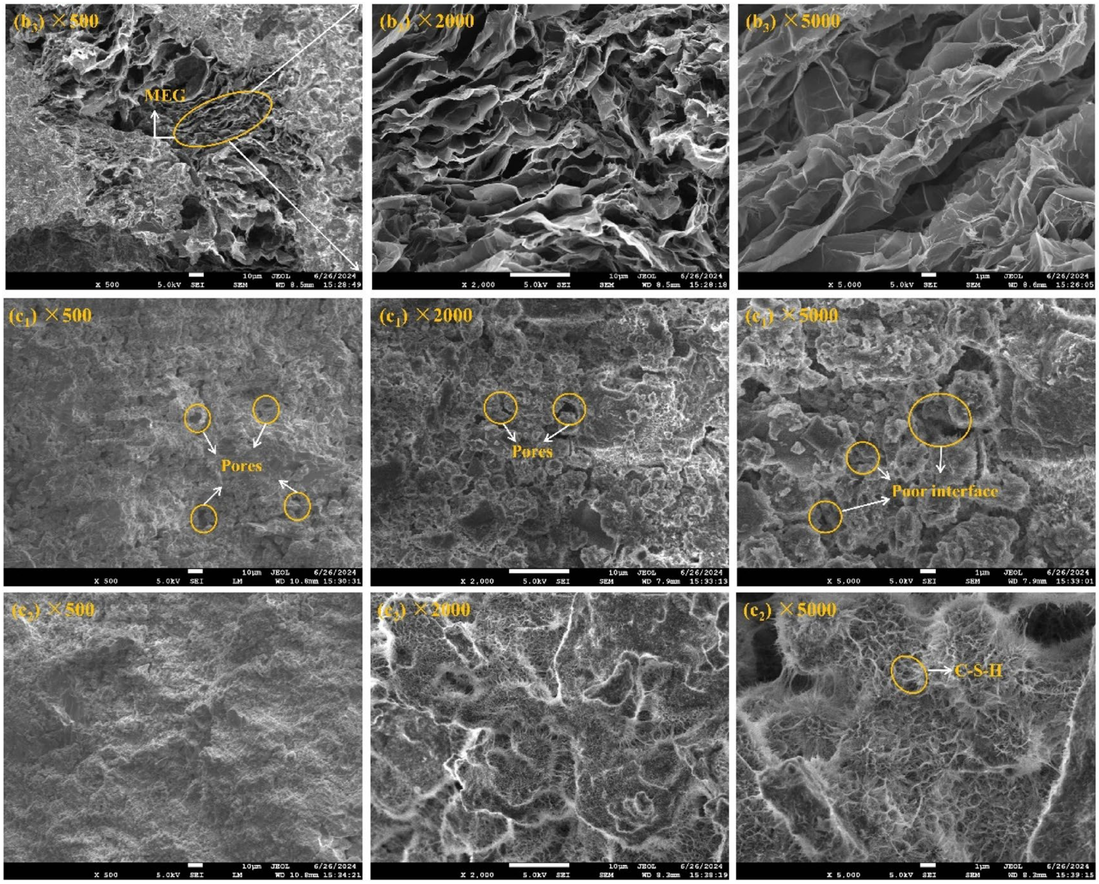

Fig. 14. (continued)

On the contrary, the MEG-cement in Fig. 14 (a_2, b_2, c_2) has a flat and dense structure. There are numerous clustered C-S-H gels visible at a multiple of ×5000. Following its passage through C-S-H, the needle-shaped AFt also developed a solid non-porous structure. EP fills three-dimensional honeycomb graphite at the nanoscale, with a complete structure at ×5000, as shown in Fig. 14 (b_3). Through epoxy groups at the end of molecular chains, EP can coordinate and chelate with Ca^{2+} in cement, facilitating the precipitation of crystalline products like $Ca(OH)_2$ and C-S-H. The absence of a visible microcrack between MEG and hydration products suggests that MEG-cement has a denser structure and better binding than G-cement. In conclusion, SEM imaging verifies that MEG has effectively reduced the overall porosity and precisely controlled the spatial distribution of microscale holes to create a "high connectivity, low tortuosity" heat conduction network.

MIP

Mercury intrusion porosimetry (MIP) is used to quantitatively determine the pore size distribution (PSD) of hardened cement and construct a correlation with heat transfer efficiency. The PSD curves for G-cement and MEG-cement are shown in Fig. 15. The porosity of MEG-cement dropped from 48.6222 to 38.1148 in comparison to G-cement, and the peak value at about 1000 nm decreased from 0.257 cc/g to 0.223 cc/g. The Mode value decreased from 1.653 μm to 1.199 μm. It is reported that the pores in cement can be classified as macropores (> 1 μm), capillary pores (0.1 ~ 1 μm), transition pores (0.01–0.1 μm), and gel pores (< 0.01 μm)[70]. Table 4 illustrates that the gel pore content of MEG-cement significantly decreased from 5.84 to 0.21% upon the addition of MEG. It was confirmed that MEG induced C-S-H gel to densify and accumulate, and its interlayer pores were effectively filled by low molecular weight materials. The proportion of transition pores was also reduced by 15.13% compared with the control group. Based on the analysis of FT-IR and SEM, this indicated that MEG promoted the formation of C-S-H gel and filled the micropores.

The proportion of capillary pores with pore sizes ranging from 0.1 to 1 μm in MEG-cement was higher than that of the control group. Hence, the median diameter (D_{50}) of MEG-cement (0.5714 μm) was higher than the control group (0.2753 μm). The average diameter of MEG-cement (0.1025 μm) was also higher than the control group (0.0461 μm). Tavman and Fuchs et al. found that the larger the pores in the rock, the smaller the surface area of the pores, and the shorter the heat transfer path, resulting in a higher thermal conductivity[71,72]. Also, this is the main reason for the decreased strength and density in MEG-cement. In short, the quantitative analysis presented by MIP provides additional support for the findings derived from SEM observations.

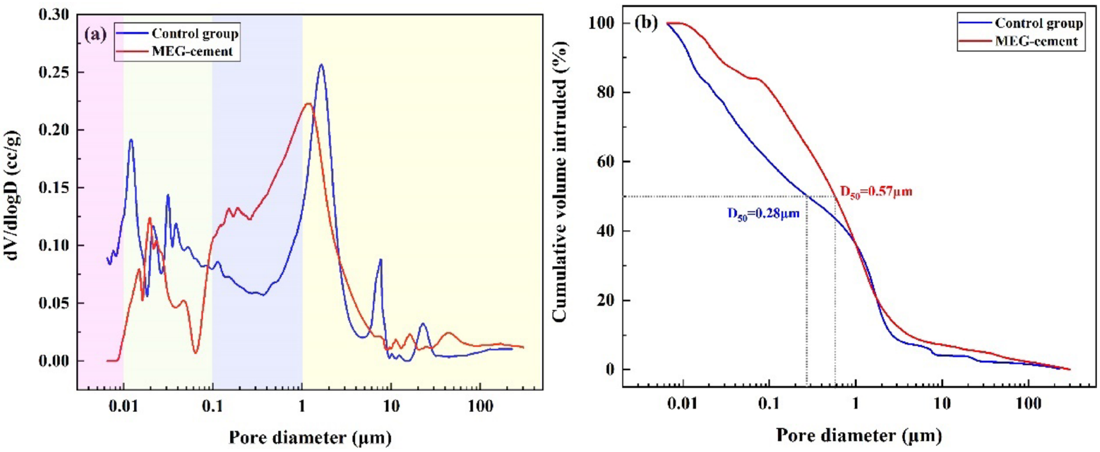

Fig. 15. Pore size analysis of cement samples: (**a**) pore size distribution; (**b**) cumulative curve.

Sample	Gel pore (< 0.01 μm)	Transition pore (0.01 ~ 0.1 μm)	Capillary pores (0. 1 ~ 1 μm)	Macropore pores (> 1 μm)
G-cement	5.84%	34.02%	23.80%	36.34%
MEG-cement	0.21%	18.89%	44.66%	36.24%

Table 4. Pore size distribution of G-cement and MEG-cement.

Mechanism analysis

Phonon, photon, and electron thermal conduction are the primary techniques used in solid materials. Cement as a composite material made of inorganic porous media, thermal conduction primarily uses phonon heat transfer, or lattice vibration, to move energy from the high-temperature zone to the low-temperature region[17]. The thermal conductivity of pores filled with gas is much lower than that of the cement matrix; therefore, the filling of pores and the penetration of thermal conductivity channels have become the principles of thermal conductivity enhancement design in this study. By establishing a "molecular-mesoscopic-macroscopic" correlation, the synergistic mechanism of MEG cement was revealed:

The addition of MEG secured the hydration progress and produced a number of hydration products that mixed well with the aggregate, including rod-needle AFt, cluster gel, dense honeycomb MEG, plate $Ca(OH)_2$, etc. Concurrently, the solidified EP in MEG can chelate by coordinating with the Ca^{2+} in the cement matrix, facilitating the precipitation of crystal products such $Ca(OH)_2$, converting C_2S/C_3S to C-S-H gel, and promoting the directed growth of epitaxy at the pore interface.

At the mesoscopic scale, MEG-cement significantly reduces the crack, total porosity, gel pore, and transition pore content in the interface transition zone and increases the pore ratio of > 0.1 μm. The smaller the specific surface area of pores, the shorter the heat transfer path. This directional pore distribution optimization is qualitatively/quantitatively confirmed by SEM and MIP tests.

By guiding hydration products and controlling the spatial distribution of micropores, MEG efficiently increases the connectedness of the cement matrix at the macro scale, creating a "high connectivity, low tortuosity" heat conduction network, as seen in Fig. 16. With an increase in the thermal conductivity coefficient of up to 20.7–182.1%, the present MEG system has made history in the synergistic effect of mechanical characteristics, engineering properties, and thermal conductivity for the first time in harsh environments of 60–100 °C and ≤ 36% NaCl. This study provides a viable paradigm for the construction of new high thermal conductivity fillers by confirming that it is feasible to bridge and fill the three-dimensional pores of conventional carbon-based materials using the complexation concept.

Conclusion

In response to the dual challenges of insufficient thermal conductivity of cement sheaths to suppress downhole heat transfer efficiency and degradation of cement properties by traditional thermal conductive fillers, this study successfully designed and synthesized a new composite material (MEG) of expanded graphite/epoxy resin through an ion complexation mechanism, comprehensively demonstrating its applicability in enhancing thermal conductivity of geothermal cement and revealing the mechanism. Through systematic experiments and multi-scale characterization, the following conclusions are drawn:

(1) Theoretical contribution: the use of ZDMA to stimulate the ring-opening reaction of EP and create a stable cation-π bridging interaction with EG was a novel theoretical contribution. This process offers fresh concepts for the composite design of porous materials and polymers by explaining the fundamentals of the dense structure and superior thermal stability created by the epoxy resin filling of EG honeycomb pores.

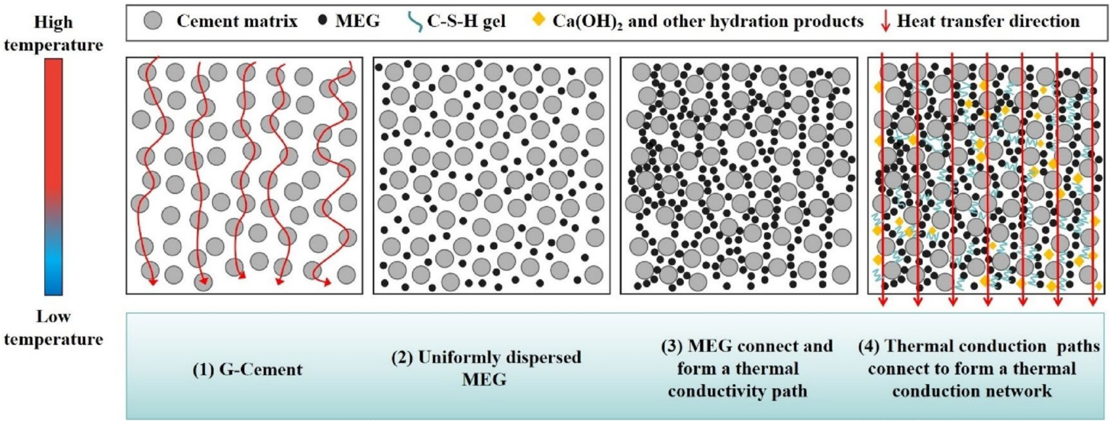

Fig. 16. Schematic diagram of the mechanism of MEG improving the cement thermal conductivity.

Furthermore, by offering C-S-H gel reaction sites, MEG encourages the nucleation of C-S-H gel and fills the cement skeleton's transition and gel pores, creating a network of dense, high thermal conductivity. This founding deepens the theoretical understanding of the synergistic mechanism between cement hydration, pore structure, and thermal conductivity.

(2) Practical value: in high-temperature environments (60–100 ℃), the optimal addition of MEG is 5–10%. The thermal conductivity of MEG-cement has increased to 0.1359–0.2694 W/(m·K), with an increment (ITC) of 46.6–182.1%, while ensuring that the compressive strength (≥ 10.3 MPa) and flowability (variation $\leq 5\%$) meet the API standards. The high thermal conductivity (0.1422–0.1899 W/(m·K)) of MEG-cement under high salt conditions (5–36% NaCl) provides an economic solution for high salinity geothermal wells.

(3) Directions for optimization: results show that excess MEG (> 10%) causes interface flaws, which continuously reduce compressive strength. The ITC also dropped by 4.8%, 48%, and 67.7% at 60 °C, 80 °C, and 100 °C, respectively. Hence, by controlling the material's dispersibility and contact angle, the compatibility between the MEG filler and the cement matrix should be maximized.

(4) Research limitations and prospects: MEG-cement reduces compressive strength (by 35%) while maintaining ITC stability in an NaCl environment. Next, the development of MEG-nano SiO_2 and other composite systems will be carried out to synergistically enhance mechanical properties. On the other hand, current simulation experiments are limited to static salt solutions, and future research will consider increasing the coupling effect of corrosive media such as CO_2/H_2S.

Data availability

The datasets used and/or analyzed during the current study are available from the corresponding author on reasonable request.

Received: 26 February 2025; Accepted: 11 June 2025

References

1. Zhonghe, P., Shengbiao, H. & Jiyang, W. A. Roadmap to geothermal energy development in China. *Sci. Technol. Rev.* **30**, 18–24 (2012).
2. Kremieniewski, M., Jasinski, B., Zima, G. & Kut, L. Reduction of fractionation of lightweight slurry to geothermal boreholes. *Energies* **14** https://doi.org/10.3390/en14123686 (2021).
3. Aziz, Z. S. et al. Bacterial biodegradation of oil-contaminated soil for pollutant abatement contributing to achieve sustainable development goals: A comprehensive review. *Results Eng.* **22**, 102083. https://doi.org/10.1016/j.rineng.2024.102083 (2024).
4. Abdelzaher, M. A. & Awad, M. M. Sustainable development goals for the circular economy and the Water-Food nexus: full implementation of new drip irrigation technologies in upper Egypt. *Sustainability* **14**, 13883. https://doi.org/10.3390/su142113883 (2022).
5. Abdelzaher, M. A., Farahat, E. M., Abdel-Ghafar, H. M., Balboul, B. A. A. & Awad, M. M. Environmental policy to develop a conceptual design for the Water–Energy–Food nexus: A case study in Wadi-Dara on the red sea coast, Egypt. *Water* **15**, 780. https://doi.org/10.3390/w15040780 (2023).
6. Arbad, N., Emadi, H. & Watson, M. A comprehensive review of geothermal cementing from well integrity perspective. *J. Petrol. Sci. Eng.* **217** https://doi.org/10.1016/j.petrol.2022.110869 (2022).
7. Won, J., Choi, H. J., Lee, H. & Choi, H. Numerical investigation on the effect of cementing properties on the thermal and mechanical stability of geothermal wells. *Energies* **9** https://doi.org/10.3390/en9121016 (2016).
8. Wu, Y., Patel, H. & Salehi, S. Parametric study of mechanical stresses within cement sheath in geothermal wells. *Geoth* **90** https://doi.org/10.1016/j.geothermics.2020.102000 (2021).
9. Sugama, T. & Brothers, L. E. Sodium-silicate-activated slag for acid-resistant geothermal well cements. *Adv. Cem. Res.* **16**, 77–87. https://doi.org/10.1680/adcr.16.2.77.36256 (2004).
10. Palou, M. & Bagel, L. u. Preparation and properties of cementitious composites for geothermal applications. *Chemical Papers* 66, 881–890, (2012). https://doi.org/10.2478/s11696-012-0166-y
11. Childers, M. I. et al. Polymer-Cement composites with Self-Healing ability for geothermal and fossil energy applications. *Chem. Mater.* **29**, 4708–4718. https://doi.org/10.1021/acs.chemmater.7b00344 (2017).

12. Song, X. et al. Performance study of the downhole coaxial Closed-Loop heat exchange technology in Xiongan new area. *J. Tianjin Univ.* **54**, 971–981 (2021).
13. Li, R. et al. Numerical analysis of the effect of cement sheath on the heat extraction performance of coaxial borehole heat exchangers geothermal system. *Build. Sci.* **34**, 36–40 (2018).
14. Yang, Y. et al. Calculation model and influence factors of thermal conductivity of composite cement-based materials for geothermal well. *Geotherm. Energy*. **12** https://doi.org/10.1186/s40517-024-00282-w (2024).
15. Han, Y. et al. Influencing patterns of multiple factors on the heat transfer performance of moderately deep geothermal wells. *Coal Geol. Explor.* **52**, 104–116 (2024).
16. Zhang, F. & Li, L. Study on thermal conductivity of thermal insulation cement in geothermal well. *Front. Earth Sci.* **10** https://doi.org/10.3389/feart.2022.784245 (2022).
17. Wang, S., Jian, L., Shu, Z., Chen, S. & Chen, L. A high thermal conductivity cement for geothermal exploitation application. *Nat. Resour. Res.* **29**, 3675–3687. https://doi.org/10.1007/s11053-020-09694-4 (2020).
18. Bao, X., Memon, S. A., Yang, H., Dong, Z. & Cui, H. Thermal properties of Cement-Based composites for geothermal energy applications. *Materials* **10** https://doi.org/10.3390/ma10050462 (2017).
19. Song, X. et al. Study on thermal conductivity of cement with thermal conductive materials in geothermal well. *Geoth* **81**, 1–11. https://doi.org/10.1016/j.geothermics.2019.04.001 (2019).
20. Li, Y. et al. Investigation on the synergy enhancement effect and mechanism of consolidation/thermal conductivity of CNTs-composite cement. *Geoth* **115** https://doi.org/10.1016/j.geothermics.2023.102809 (2023).
21. Li, B., Zhang, J., Yan, H., Liu, H. & Zhu, C. Thermal enhancement of gangue-cemented paste backfill with graphite and silica sand: an experimental investigation. *Environ. Sci. Pollut. Res.* **29**, 49050–49058. https://doi.org/10.1007/s11356-022-19305-9 (2022).
22. Guo, S. Y. et al. Mechanical and interface bonding properties of epoxy resin reinforced Portland cement repairing mortar. *Constr. Build. Mater.* **264** https://doi.org/10.1016/j.conbuildmat.2020.120715 (2020).
23. Guo, S. Y. et al. Preparation of TiO_2/epoxy resin composite and its effect on mechanical and bonding properties of OPC mortars. *Constr. Build. Mater.* **272** https://doi.org/10.1016/j.conbuildmat.2020.121960 (2021).
24. Chen, S. et al. An experimental and theoretical study of biomimetic cement-epoxy resin composites: structure, mechanical properties, and reinforcement mechanisms. *Compos. Part. a-Applied Sci. Manuf.* **185** https://doi.org/10.1016/j.compositesa.2024.108297 (2024).
25. Ji, Y. et al. Performance evaluation of geothermal cementing materials based on orthogonal tests. *J. Mater. Sci. Eng.* **40**, 1018–1024 (2022).
26. Zhang, D., Zhang, W., Zhang, S., Ji, X. & Li, L. Synthesis of expanded graphite-based materials for application in lithium-based batteries. *J. Energy Storage*. **60** https://doi.org/10.1016/j.est.2023.106678 (2023).
27. Shuping, W. et al. Recent progress about expanded graphite matrix composite phase change material for energy storage. *Energy Storage Sci. Technol.* **3**, 210–215 (2014).
28. Xu, F. et al. Outstanding thermally conductive and anticorrosive polymer composite coating via a multifunctional epoxy curing agent zinc dimethacrylate. *Chem. Eng. J.* **473** https://doi.org/10.1016/j.cej.2023.145163 (2023).
29. Zhao, G. & Zhu, H. Cation-π interactions in Graphene-Containing systems for water treatment and beyond. *Adv. Mater.* **32** https://doi.org/10.1002/adma.201905756 (2020).
30. Mahadevi, A. S. & Sastry, G. N. Cation-π interaction: its role and relevance in chemistry, biology, and material science. *Chem. Rev.* **113**, 2100–2138. https://doi.org/10.1021/cr300222d (2013).
31. Di, B. *Preparation and Properties of High Thermal Conductivity Epoxy-based Composites* Doctoral thesis, Northeast Petroleum University, (2022).
32. Zhu, W., Wang, B., Cui, S., Tan, H. & Yang, S. Study on the improvement of geothermal cement properties by nanofluid composed of deep eutectic solvent and graphene oxide. *Sci. Rep.* **14** https://doi.org/10.1038/s41598-024-80012-1 (2024).
33. Sugama, T. & Pyatina, T. Effect of sodium carboxymethyl celluloses on water-catalyzed self-degradation of 200°C-heated alkali-activated cement. *Cem. Concr Compos.* **55**, 281–289. https://doi.org/10.1016/j.cemconcomp.2014.09.015 (2015).
34. Tan, H. et al. Light-weight temporary-sealing cement for medium temperature geothermal wells by using Polyvinyl alcohol fibers and fly Ash cenospheres. *J. Petrol. Sci. Eng.* **215** https://doi.org/10.1016/j.petrol.2022.110704 (2022).
35. Gul, S., Aslanoglu, V., Tuzen, M. K. & Senturk, E. in *44th Workshop on Geothermal Reservoir Engineering* 1–7.
36. García, A., Santoyo, E., Espinosa, G., Hernández, I. & Gutiérrez, H. Estimation of temperatures in geothermal wells during circulation and Shut-in in the presence of lost circulation. *TPM* **33**, 103–127. https://doi.org/10.1023/A:1006545610080 (1998).
37. Saito, S. The status of deep geothermal well drilling in kakkonda, Japan. *J. Jpn Assoc. Pet. Technol.* **50**, 353–362 (1993).
38. Weihong, Z., Qunxi, Z. & Siping, H. Study on Preparation of Nano-ZnO with different sizes and their ability to resist ultraviolet ray. *Guangdong Chem. Ind.* **22**, 10–12 (2018).
39. Qiaoyun, L., Xuelin, W. & Shuping, S. Infrared spectroscopic qualitative study of carboxylic acid and carboxylate structure. *Nat. Sci. J. Harbin Normal Univ.* **12**, 67–70 (1996).
40. Lin, Y. et al. The use of zinc dimethacrylate functionalized graphene as a reinforcement in rubber composites. *Polym. Adv. Technol.* **26**, 423–431. https://doi.org/10.1002/pat.3424 (2015).
41. Demongeot, A., Mougnier, S. J., Okada, S., Soulie-Ziakovic, C. & Tournilhac, F. Coordination and catalysis of Zn^{2+} in epoxy-based vitrimers. *Polym. Chem.* **7**, 4486–4493. https://doi.org/10.1039/c6py00752j (2016).
42. Yu, C. *Experimental Investigation of Green Preparation and Application for Expanded Graphite* Master thesis, Yanshan University, (2021).
43. Qi, B. et al. Strong Co-Ion effect via Cation-π interaction on the Self-Assembly of Metal-Organic cationic macrocycles. *J. Am. Chem. Soc.* **139**, 12020–12026. https://doi.org/10.1021/jacs.7b06564 (2017).
44. Cheng, F. et al. A novel function-designed carbon fiber reinforced polymer with implanting expanded graphite/paraffin composite into interlayers: mechanical, thermal and sustainable properties analysis. *Compos. Sci. Technol.* **188** https://doi.org/10.1016/j.compscitech.2019.107965 (2020).
45. Jin, H. et al. Comparative tribological behavior of friction composites containing natural graphite and expanded graphite. *Friction* **8**, 684–694. https://doi.org/10.1007/s40544-019-0293-3 (2020).
46. Cui, L., Shi, S., Li, Z., Wei, G. & Du, X. Manipulating thermal conductance of supported graphene via surface hydroxylation of substrates. *J. Phys. Chem. C.* **122**, 27689–27695. https://doi.org/10.1021/acs.jpcc.8b07873 (2018).
47. Xiujuan, T., Wenge, W., Qiang, Z. & Qingkun, H. Application of thermal analysis technique in the study of thermosetting resins. *Shandong Chem. Ind.* **48**, 12–15 (2019).
48. Wei, J. et al. Extremely high thermal conductive cement-based composites with diamond/zno/expanded graphite thermal conductivity network for cooling road. *Constr. Build. Mater.* **393** https://doi.org/10.1016/j.conbuildmat.2023.131968 (2023).
49. Wang, S. et al. Investigation on thermal conductivity property and hydration mechanism of graphene-composite cement for geothermal exploitation. *Geoth* **104** https://doi.org/10.1016/j.geothermics.2022.102477 (2022).
50. Xue, Q. et al. Thermal conductivity and pore structure analysis of alkali-activated foam cement with supercritical CO2 modified slag: feasibility evaluation for geothermal applications. *Constr. Build. Mater.* **347** https://doi.org/10.1016/j.conbuildmat.2022.128506 (2022).
51. Jin-yang, Y., Zhan-xue, B., Xiu-hua, Z. & Dan, Z. Fei-yue, L. Controlled pressure drilling and the application in High-temperature geothermal exploration. *Explor. Eng. (Rock Soil. Drill. Engineering)*. **40**, 19–23 (2013).

52. Duan, R., Li, P., Wang, L., He, X. & Zhang, L. Hydrochemical characteristics, hydrochemical processes and recharge sources of the geothermal systems in Lanzhou city, Northwestern China. *Urban Clim.* **43** https://doi.org/10.1016/j.uclim.2022.101152 (2022).
53. Li, X., Huang, X., Liao, X. & Zhang, Y. Hydrogeochemical characteristics and conceptual model of the geothermal waters in the Xianshuihe fault zone, Southwestern China. *Int. J. Env Res. Public. Health.* **17** https://doi.org/10.3390/ijerph17020500 (2020).
54. Yin, H. et al. Hydrochemical characteristics and genetic mechanism of porous sandstone geothermal water in Northern jinan, shandong, China. *Environ. Sci. Pollut. Res.* https://doi.org/10.1007/s11356-024-32714-2 (2024).
55. Zhongping, W., Haoyu, Y., Yating, Z. & Linglin, X. Effect of sodium chloride on hydration of calcium aluminate cement at different temperatures. *Mater. Rep.* **33**, 2343–2347 https://doi.org/10.11896/cldb.18050307 (2019).
56. Maagi, M. T. & Jun, G. Effect of the particle size of Nanosilica on early age compressive strength in oil-well cement paste. *Constr. Build. Mater.* **262** https://doi.org/10.1016/j.conbuildmat.2020.120393 (2020).
57. Wang, C., Wang, L., Geng, C. & Yao, X. Benefits of delayed addition of Rutin on the thickening time and compressive strength of oil well cement. *Constr. Build. Mater.* **322** https://doi.org/10.1016/j.conbuildmat.2021.126287 (2022).
58. Zhu, J., Wei, J., Yu, Q., Xu, M. & Luo, Y. Hybrid effect of wollastonite Fiber and carbon Fiber on the mechanical properties of oil well cement pastes. *Adv. Mater. Sci. Eng.* **2020** https://doi.org/10.1155/2020/4618035 (2020).
59. Abdelzaher, M. A. Sustainable development goals for industry, innovation, and infrastructure: demolition waste incorporated with nanoplastic waste enhanced the physicomechanical properties of white cement paste composites. *Appl. Nanosci.* **13**, 5521–5536. https://doi.org/10.1007/s13204-023-02766-w (2023).
60. Zhang, G., Zhao, J., Wang, P. & Xu, L. Effect of HEMC on the early hydration of Portland cement highlighted by isothermal calorimetry. *JTAC* **119**, 1833–1843. https://doi.org/10.1007/s10973-014-4346-6 (2015).
61. Wang, R., Yao, L. & Wang, P. Mechanism analysis and effect of styrene-acrylate copolymer powder on cement hydrates. *Constr. Build. Mater.* **41**, 538–544. https://doi.org/10.1016/j.conbuildmat.2012.12.028 (2013).
62. Tan, H., He, W., Ye, Y., Chen, Y. & Zheng, X. Influence of Polyvinyl alcohol coated porous Al_2O_3 ceramic waste particles on cement properties in geothermal applications. *Constr. Build. Mater.* **376**, 1–11. https://doi.org/10.1016/j.conbuildmat.2023.131046 (2023).
63. Kupwade-Patil, K., Palkovic, S. D., Bumajdad, A., Soriano, C. & Buyukozturk, O. Use of silica fume and natural volcanic Ash as a replacement to Portland cement: Micro and pore structural investigation using NMR, XRD, FTIR and X-ray microtomography. *Constr. Build. Mater.* **158**, 574–590. https://doi.org/10.1016/j.conbuildmat.2017.09.165 (2018).
64. Trezza, M. A. Hydration study of ordinary Portland cement in the presence of zinc ions. *Mater. Res.* **10**, 331–334. https://doi.org/10.1590/s1516-14392007000400002 (2007).
65. Abbas, R., Abdelzaher, M. A., Shehata, N. & Tantawy, M. A. Production, characterization and performance of green geopolymer modified with industrial by-products. *Sci. Rep.* **14**, 5104. https://doi.org/10.1038/s41598-024-55494-8 (2024).
66. Tao, S., Zeping, Y. & Liwei, Z. FTIR spectra for early age hydration of cement-based composites incorporation with CNTs. *AcMCS* **34**, 653–660. https://doi.org/10.13801/j.cnki.fhclxb.20160607.024 (2017).
67. Rui, Z. et al. Study on factors affecting thermal conductivity of thermal conductive cement in geothermal well. *ACTA Energiae Solaris Sinica*. **42**, 10–15. https://doi.org/10.19912/j.0254-0096.tynxb.2019-0050 (2021).
68. Yang, Y. et al. Study on the performance and mechanism of high thermal conductivity and low-density cementing composite for deep geothermal wells. *Energy* **285** https://doi.org/10.1016/j.energy.2023.129429 (2023).
69. Abdelzaher, M. A., Hamouda, A. S. & El-Kattan, I. M. A comprehensive study on the fire resistance properties of ultra-fine ceramic waste-filled high alkaline white cement paste composites for progressing towards sustainability. *Sci. Rep.* **13**, 22097. https://doi.org/10.1038/s41598-023-49229-4 (2023).
70. Yu, Y. et al. Preparation, properties and structure of high heat conduction and low density cementing materials for geothermal wells. *Drill. Fluid Completion Fluid*. **38**, 93–101 (2021).
71. Tavman, I. H. Effective thermal conductivity of granular porous materials. *ICHMT* **23**, 169–176. https://doi.org/10.1016/0735-1933(96)00003-6 (1996).
72. Fuchs, S. & Foerster, A. Rock thermal conductivity of mesozoic geothermal aquifers in the Northeast German basin. *Chemie Der Erde-Geochemistry*. **70**, 13–22. https://doi.org/10.1016/j.chemer.2010.05.010 (2010).

Acknowledgements

This research has been funded by the China Postdoctoral Science Foundation (Grant No. 2023M730947), the Key Laboratory of Shallow Geothermal Energy, Ministry of Natural Resources of the People's Republic of China, No. KLSGE202501-03, Key Scientific Research Project of Higher Education Institutions in Henan Province (25B440001), Open research projects for undergraduate students in research laboratories (platforms) in 2024 (20242802063), and Sichuan Science and Technology Program (grant number 2023NSFSC0781).

Author contributions

Wenxi Zhu: Funding acquisition, writing-original draft.Bingjie Wang: Data curation.Shengkai Cui: Investigation, Methodology.Jing Wang: Image processing.Huijing Tan: Writing-review & editing, Funding acquisition.

Declarations

Competing interests

The authors declare no competing interests.

Additional information

Correspondence and requests for materials should be addressed to W.Z.